PAPER

Novel Li$_2$MnO$_3$ nanowire anode with internal Li-enrichment for use in a Li-ion battery†

Dandan Wang,‡ Yunlong Zhao,‡ Xu Xu, Kalele Mulonda Hercule, Mengyu Yan, Qinyou An, Xiaocong Tian, Jiaming Xu, Longbing Qu and Liqiang Mai*

Anode materials which undergo a conversion reaction can achieve larger specific capacities than conventional carbon-based materials. They can even achieve higher energy densities when used at low voltages. However, the large amounts of Li$_2$O generated in the interior of these structures when Li ions are inserted can cause volume expansion and mechanical fracturing from the inside out. This leads to a poor cycling performance and limits their commercial application. To overcome this limitation, we introduced Li ions into the interior of the cells of manganese oxide materials and successfully synthesized a novel Li-rich anode material (Li$_2$MnO$_3$). The reversible capacity reached 1279 mA h g^{-1} after 500 cycles, much higher than that of pure MnO$_2$ or other commercial anodes. This optimization of the internal Li-enrichment and its application in Li$_2$MnO$_3$ nanowires used as low voltage anodes in Li-ion batteries have rarely been reported. Further investigations by X-ray diffraction and photoelectron spectroscopy suggested that the strategy of optimizing the internal Li-enrichment of this novel Li$_2$MnO$_3$ anode is a promising development for Li-ion batteries.

Introduction

The current need for rechargeable lithium-ion batteries (LIB) with high power and energy density has led to much interest in the use of nanotechnology to obtain high-performance, low-cost and environmentally friendly electrode (cathode/anode) materials.[1–9] As anode materials for LIB, the transition metal oxides, such as Cr$_2$O$_3$,[10] Fe$_2$O$_3$,[11] Co$_3$O$_4$,[12–14] CuO[15] and MnO$_2$ (ref. 16) have many advantages compared with conventional carbon-based materials. MnO$_2$ has long been studied as a cathode material for LIB and as an electrode material for super-capacitors because of its natural abundance, non-toxicity and cost effectiveness.[17–21] As a typical transition metal oxide, MnO$_2$ can also serve as a potential anode material; if all its possible oxidation states are used through a conversion reaction, it possesses a high theoretical capacity of four electron transfers per manganese ion. However, a poor cycling performance limits its application as an anode material for LIB. As shown in Fig. 1a (left), MnO$_2$ is compact before charging–discharging. After the insertion of Li ions into the crystal structure and their conversion reaction with MnO$_2$, Mn and Li$_2$O nanoparticles are formed electrochemically *in situ*. However, serious crystal

distortion and volume expansion lead to lattice stress and self-aggregation during the charge–discharge cycle (Fig. 1a, right), resulting in a loss of electrical contact and ultimately electrode failure.[22,23]
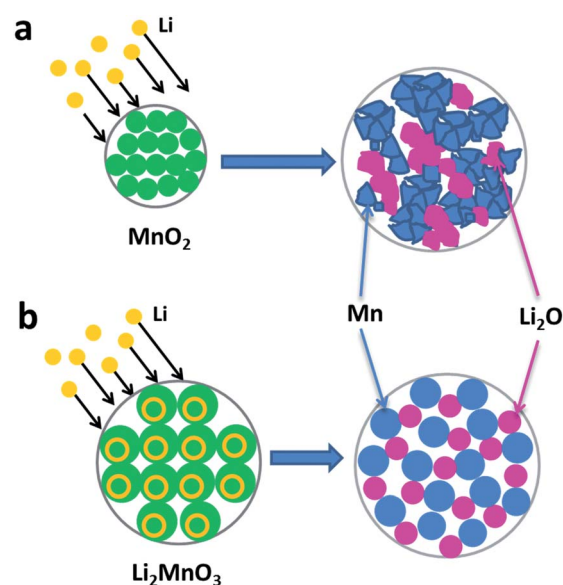

Fig. 1 Schematic illustration of the behavior of (a) a MnO$_2$ electrode showing the failure of the electrode because of crystal lattice and volume changes. (b) Our internal Li-enriched Li$_2$MnO$_3$ anode electrode showing well-maintained electrical contact between the metallic Mn nanoparticles and Li$_2$O.

State Key Laboratory of Advanced Technology for Materials Synthesis and Processing, WUT-Harvard Joint Nano Key Laboratory, Wuhan University of Technology, Wuhan, 430070, P. R. China. E-mail: mlq518@whut.edu.cn; Fax: +86-27-87644867; Tel: +86-27-87467595

‡ These authors contributed equally to this work.

Previous strategies used to overcome these problems include: (1) reducing the particle size from the microscale to the nanoscale to accommodate the large volume change and shorten the diffusion length of the Li ion;[24] (2) coating carbon-based materials or conducting polymers to enhance the electronic conductivity;[25–30] and (3) constructing hierarchical nanocomposites to take full advantage of the synergistic effect of the different components.[31–35] These techniques can partly prevent the large volume expansion and the resultant loss of electrical contact, but they are all forms of external modification and the crystal deformation and volume change still occur. Moreover, even sophisticated synthetic processes cannot stop the inevitable fading of the reversible specific capacity with time.

However, if we introduce Li ions into the intracell of these anode materials to obtain a Li_xMO_y structure (Fig. 1b), the M metal electrochemically formed *in situ* (specifically Mn in this case) and Li_2O are dispersed during the conversion process and occupy a larger space, which buffers the volume expansion. Furthermore, this Li-enrichment removes the requirement that the cathode must contain Li in its original state and opens up new opportunities for pairing Li-free electrodes for the next generation of high-energy LIB.[36] Although similar strategies, such as prelithiation, have been applied in intercalation reactions to increase the ionic diffusion and/or electronic conductivity of anode materials,[37–39] to the best of our knowledge this strategy and its function have rarely been reported in the conversion reactions of anode materials.

In the work reported here, we successfully synthesized a novel Li-rich anode material (Li_2MnO_3) for LIB by inserting Li ions into manganese oxide. In contrast with the rapid fading of the capacity of MnO_2, Li_2MnO_3 exhibits a very stable cycling performance and has a capacity of over 1200 mA h g^{-1}, much higher than conventional carbon-based materials and other commercial anodes. Studies using X-ray diffraction (XRD), modeling and X-ray photoelectron spectroscopy (XPS) revealed that the Li pre-inserted in the MnO_2 lattice plays a key role in stabilization. Investigations of electrochemical performance and mechanisms of action further demonstrated that both this novel and general strategy and the optimized Li_2MnO_3 anode are promising developments for LIB.

Experimental section

Materials

For a typical synthesis, $C_4H_6MnO_4 \cdot 4H_2O$, $LiOH \cdot H_2O$, H_2O_2, sodium dodecyl benzene sulfonate (SDBS) and poly(-vinylpyrrolidone) (PVP K30) were of analytical-reagent grade and were purchased from Sinopharm Chemical Reagent Co. Ltd, Shanghai, China. All chemicals were used as-received without further purification.

Methods

The Li_2MnO_3 nanowires were prepared in two stages. The MnOOH nanowires were first synthesized by a hydrothermal method. SDBS (0.769 g) and PVP K30 (0.4446 g) were dissolved

in 50 mL of deionized water. Meanwhile, $C_4H_6MnO_4 \cdot 4H_2O$ (1.725 g) and LiOH (0.555 g) were each dissolved in 15 mL of deionized water and 0.6 mL of H_2O_2 was added to each solution. The as-obtained solutions were mixed sequentially with continuous stirring. The final solution was then transferred into a 100 mL Teflon-lined stainless-steel autoclave and placed in an electric oven at 140 °C for 12 h. The autoclave was then left to cool naturally to room temperature. The precursor MnOOH nanowires obtained were centrifuged, washed several times with distilled water and ethanol, and then dried at 110 °C in a vacuum oven. In the second stage, the MnOOH nanowires and $LiOH \cdot H_2O$ were mixed (Mn : Li ratio 1 : 2) in alcohol and stirred for 12 h to obtain an homogeneous mixture. Finally, the mixture was heated at 70 °C to allow the evaporation of the alcohol and then annealed at 650 °C for 15 h in air to obtain a red powder. For comparison, the MnO_2 nanowires were also synthesized by annealing the precursor at 300 °C for 2 h (see Fig. S2 in the ESI†).

Characterizations

XRD measurements were made to investigate the crystallographic structure using a Bruker D8 Advance X-ray diffractometer with a non-monochromated Cu-Kα X-ray source. Field-emission scanning electron microscopy (FESEM) images were recorded with a JEOL JSM-7100F instrument at an acceleration voltage of 10 kV. Transmission electron microscopy (TEM) and high-resolution transmission electron microscopy (HRTEM) images were recorded using a JEOL JEM-2100F scanning transmission electron microscope instrument. X-ray photoelectron spectroscopy (XPS) measurements were obtained using a VG MultiLab 2000 instrument.

Electrochemical measurements

The electrochemical properties were measured by assembling 2016 coin cells in a glove box filled with pure argon gas. These cells used lithium pellets as the counter electrode and reference electrode and a 1 M solution of $LiPF_6$ in ethylene carbon/dimethyl carbonate (1 : 1 w/w) as the electrolyte. The anode electrodes consisted of 70% Li_2MnO_3 nanowires as the active material, 20% acetylene black and 10% poly(tetrafluoro-ethylene). Galvanostatic charge/discharge cycling was studied in the potential range 3.0–0 V *vs.* Li/Li$^+$ with a multi-channel battery testing system (LANDT CT2001A). Cyclic voltammetry (CV) and AC-impedance tests were performed using an electrochemical workstation (CHI 760D and Autolab PGSTAT 302N).

Results and discussion

XRD measurements were carried out to determine the phase structures of the as-obtained products. Fig. 2a shows the XRD patterns of the synthesized nanowires indexed as a Li_2MnO_3 monoclinic structure (JCPDS no. 00-027-1252, $a = 4.928$ Å, $b = 8533$ Å, $c = 9.604$ Å and $\beta = 99.5°$) with a space group of $C2/m$; this structure is the same as that of $R3m$ layered rock salt. TEM investigations were also carried out. As shown in Fig. 2b, the as-prepared product shows a nanowire morphology. The HRTEM
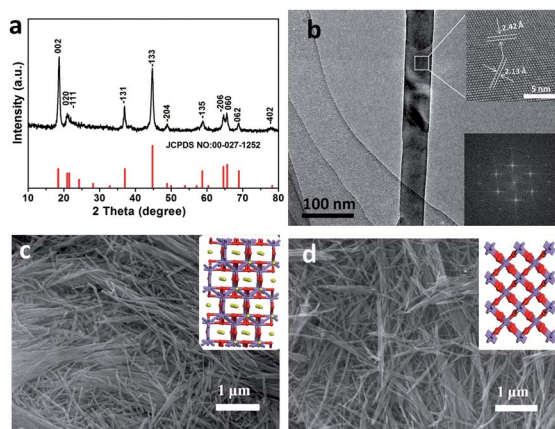
Fig. 2 (a) XRD patterns of the Li_2MnO_3 nanowires. (b) TEM image of the Li_2MnO_3 nanowires; inset, HRTEM images of the Li_2MnO_3 nanowires. (c) SEM image of the Li_2MnO_3; inset, crystal structures of Li_2MnO_3. (d) SEM image of the MnO_2; inset, crystal structures of MnO_2. The red balls represent O atoms, the purple balls represent Mn atoms and the yellow balls represent Li atoms.

investigation revealed that these nanowires have a good crystalline structure and that the lattice fringe spacings of 2.42 and 2.13 Å correspond to the inter-plane distances of (−131) and (040) of the monoclinic structure of Li_2MnO_3, respectively.

The FESEM images provide an insight into the morphology of the products. Fig. 2c shows a FESEM image of the Li_2MnO_3 nanowires, which have diameters of 20–80 nm and smooth surfaces. Fig. 2d shows the FESEM image of MnO_2 nanowires as a control experiment. These all retain the nanowire structure and are in conformity with the nanowire morphology of the precursor MnOOH, which demonstrates that the process is a morphologically conserved transformation (Fig. S1b†). The crystal structure of the Li_2MnO_3 nanowires (shown in the inset of Fig. 2c) indicates that the structure of Li_2MnO_3 is derived from a rhombohedral α-NaFeO$_2$ structure with Li and Mn occupying the Na and Fe sites, respectively. Unusually, one-third of the positions in the Mn plane are replaced by Li to form an ordered $LiMn_2$ slab. The chemical formula of this Li_2MnO_3 can be written as $\{(Li_{1/2})_{2c}(Li_1)_{4h}\}_{interslab}$ $\{(Li_{1/2})_{2b}(Mn_1)_{4g}\}_{slab}(O_1)_{4i}(O_2)_{8j}$, in which the subscripts 2c, 4h, 2b, 4g, 4i and 8j are the lattice sites occupied by the atoms in the round brackets. The sites within the Li layers are 2c and 4h, whereas the 2b site corresponds to the Li located in the $LiMn_2$ layer.[40] The volume of the cell occupied by eight Mn atoms is 398.32×10^6 pm^3. The crystal structure of the MnO_2 nanowires in the inset of Fig. 2d can be indexed to a tetragonal phase composed of single chains of the octahedral structure.[41] The total volume of four cells is 222.56×10^6 pm^3, as the volume of a cell occupied by two Mn atoms is 55.64×10^6 pm^3. The actual calculations showed that the volume of the cells with internal Li-enrichment (Li_2MnO_3) is 79.0% larger than that of MnO_2 with the same number of Mn atoms.

To explore the influence of the optimization of Li-enrichment on the electrochemical performance, coin cells were fabricated and then the CV performance, cycling and rate behaviors of Li_2MnO_3 and MnO_2 were investigated. The CV

results for Li_2MnO_3 nanowires are shown in Fig. 3a (upper panel). CV measurements were made at a sweep rate of 0.1 mV s^{-1} in the potential range of 0–3.0 V $vs.$ Li/Li$^+$ at room temperature. During the first scan, two cathodic peaks appear at 0.75 V and 0.08 V corresponding, respectively, to the reduction of Li_2MnO_3 to metallic Mn (Mn^{4+} to Mn^0) and the bivalent manganese ion (Mn^{4+} to Mn^{2+}) embedded in an amorphous matrix of Li_2O, as well as the formation of Li_2O and a solid electrolyte interphase (SEI) layer.[42] The first discharge reaction involves the destruction of the crystal structure (the amorphization of the lattice) followed by the formation of metallic nanoparticles embedded in the Li_2O matrix. One anodic peak located at 1.35 V can be seen, which indicates that the reoxidation of Mn proceeds in one step. The CV profiles of Li_2MnO_3 in the first three cycles are similar to those of the MnO_2 nanowires, but with some differences. The CV curve of Li_2MnO_3 in the third scan closely resembles that of the second scan, which demonstrates that the lithiation and delithiation processes from the second cycle are highly reversible. Nevertheless, the CV curve of MnO_2 in the third scan still shows a reduced area.

Fig. 3b and c compare the primary cycling performance of the two samples (MnO_2 nanowires and Li_2MnO_3 nanowires) at current densities of 100 and 500 mA g^{-1}, respectively. The two samples have very similar electrochemical performance with respect to the voltage platform, but the Li_2MnO_3 nanowires show a better cycling performance. The capacity of the Li_2MnO_3 nanowires decreases in the first few cycles, then increases with cycling, and finally stabilizes at 10 cycles for cell cycling at 100 mA g^{-1}. At a current density of 100 mA g^{-1}, the second cycle discharge capacities of Li_2MnO_3 and MnO_2 nanowires are 1312 and 886 mA h g^{-1}, respectively. It is obvious that a significant loss of capacity occurs over the first few cycles, which may be attributed to decomposition of the electrolyte and an irreversible phase transition.[42] However, after 50 cycles, the discharge capacity of Li_2MnO_3 nanowires still remains at 1184 mA h g^{-1}, whereas that of the MnO_2 nanowires is only 637 mA h g^{-1}. Interestingly, the capacity gradually increases with an increasing number of cycles. At a current density of 500 mA g^{-1}, even after 500 cycles, the discharge capacity of the Li_2MnO_3 nanowires is 1279 mA h g^{-1}.

The rate capability of Li_2MnO_3 was tested at various current densities in the same potential window. The battery was charged and discharged at different rates ranging from 100 to 2000 mA g^{-1} (Fig. 3d). The Li_2MnO_3 nanowire anode delivered discharge capacities of 1311, 964, 745, 601, 440 and 251 mA h g^{-1} at current densities of 100, 200, 300, 500, 1000 and 2000 mA g^{-1}, respectively. Remarkably, even after this high-rate measurement, back at a current density of 100 mA g^{-1}, the capacity reached 1422 mA h g^{-1}. This performance indicates the high reversibility of the Li_2MnO_3 nanowires. The rate performance of Li_2MnO_3 nanowires is much better than commercial carbon-based materials[43] (~375 mA h g^{-1}) and $Li_4Ti_5O_{12}$ (ref. 44) (~175 mA h g^{-1}).

It is noteworthy that the capacity of MnO_2 as an anode material gradually decays during cycling, whereas the capacity of Li_2MnO_3 continuously increases. This significant difference indicates that there are substantial changes after optimization.
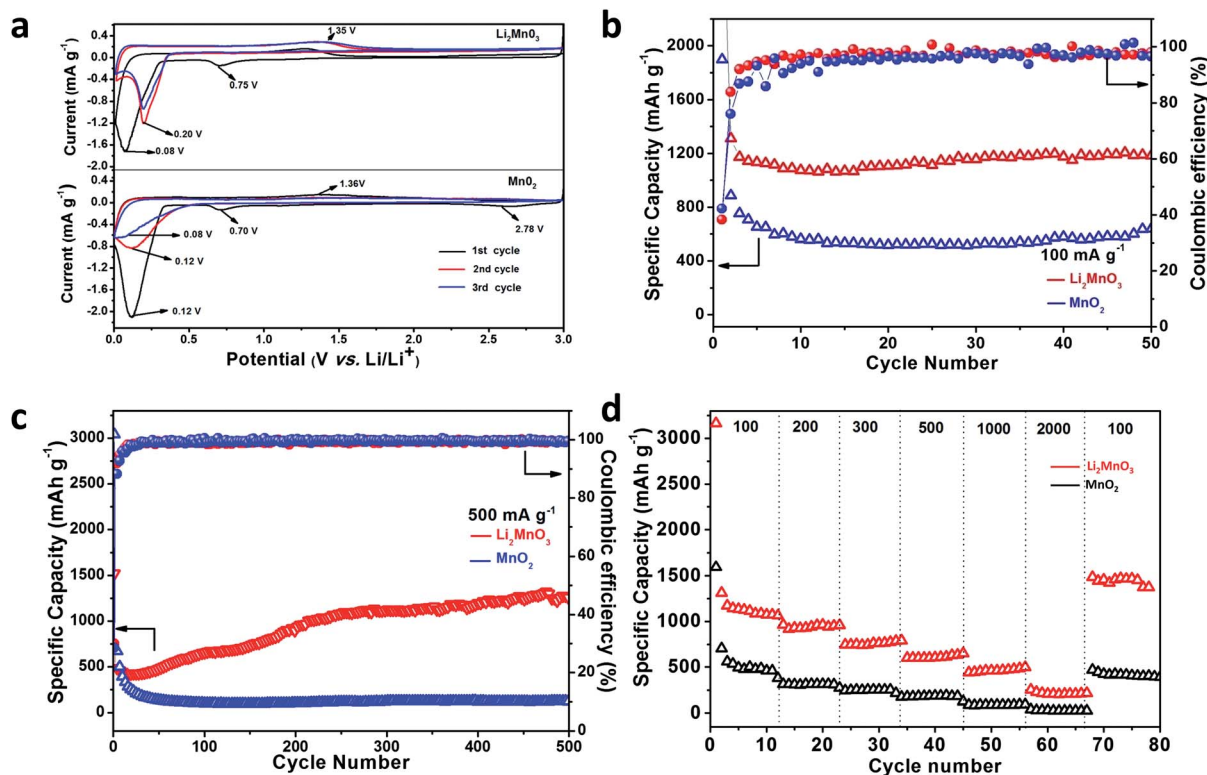
Fig. 3 (a) Cyclic voltammetry curves at a sweep rate of 0.1 mV s^{-1} in the potential range from 3.0 to 0.0 V vs. Li/Li$^+$. (b and c) Cycling performance at current densities of 100 and 500 mA g^{-1}. (d) Rate performance of Li$_2$MnO$_3$ and MnO$_2$ nanowires.

To understand the reaction mechanism of Li$_2$MnO$_3$, XPS measurements were carried out to examine the change in the oxidation state of Mn before and after lithiation (Fig. 4a). The position and line shape (sharp Mn 2p$_{3/2}$ peak at 641.9 eV and Mn 2p$_{1/2}$ peak at 653.6 eV) of the XPS spectra in Fig. 4aI once again indicate the presence of the main quadrivalent Mn ions (Mn^{4+}). The XPS spectra of the Li$_2$MnO$_3$ nanowires after lithiation (Fig. 4aII) show broader peaks of Mn 2p binding energy compared with the pristine electrode, indicating the presence of metallic Mn from the reduction of manganese oxide during the lithiation process. The XPS spectra of the Li 1s peak centered at 55.3 eV confirms the formation of Li$_2$O (inset Fig. 4aII).[16] The formation of Li$_2$O and metallic Mn during the initial lithiation process is thus confirmed, which suggests that the electrochemical reaction taking place in Li$_2$MnO$_3$ is based on a conversion reaction.

To follow the reaction process of Li$_2$MnO$_3$, the XRD patterns in three states during the first discharge process (Fig. 4b) were measured. The XRD patterns at the initial point of 3.0 V (Fig. 4bi) and 0.3 V (Fig. 4bii) show that both phases are identical to Li$_2$MnO$_3$, indicating no phase transition before 0.3 V. As reported previously, the plateau at 0.75 V is in accordance with the process associated with the reduction of the electrolyte.[45] The sloping region of the curve from 0.75 V to 0.3 V has been attributed to further SEI layer formation/electrolyte reduction on the surface of the composite electrode materials.[45] The XRD pattern measured at the end of the discharge curve (Fig. 4biii) indicates the presence of the dominant phase of Mn(OH)$_2$
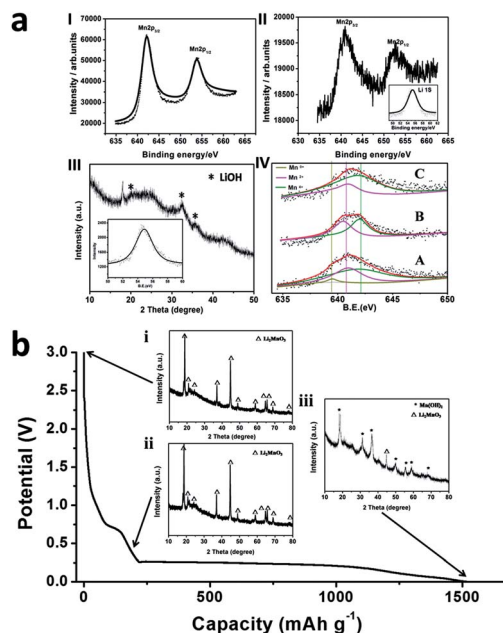

Fig. 4 (a) XPS spectra of Li$_2$MnO$_3$ nanowires (I) before the first lithium discharge process and (II) after first lithium discharge process. Formation of Mn metal and Li$_2$O during the discharge process has been confirmed using XPS. (III) XRD and XPS patterns of LiOH. (IV) Mn 2p XPS spectra of (A) first lithium discharge, (B) first lithium charge and (C) 200th lithium charge. (b) XRD patterns collected at various states of discharge for Li$_2$MnO$_3$ nanowires.

(associated with a small amount of Li_2MnO_3). Based on the XPS data, metallic Mn also exists in the final product (because of the small size of metallic Mn, no diffraction peak is detected in the XRD pattern[46]). We therefore propose the following reaction:

$$Li_2MnO_3 + 2Li^+ + H^+ + 3e^- \rightarrow$$
$$xMn + (1-x)\,Mn(OH)_2 + 2Li_2O\ (0 < x < 1) \quad (1)$$
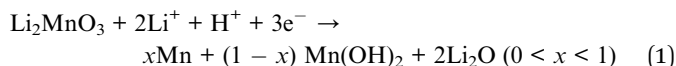
After the insertion of 2Li, the gradual decrease in the discharge voltage is associated with the decrease in LiOH (Fig. 4aIII). Thus a major reaction that contributes to the additional capacity in the Li/Li_2MnO_3 system involves the conversion reaction:

$$LiOH + 2Li^+ + 2e^- = Li_2O + LiH \quad (2)$$

which is at least partially reversible. These results for the contribution from H^+ and the formation of LiH agree well with those reported previously.[47]

To reveal the chemical changes during the cycling of Li_2MnO_3 and to further understand the enhanced cycling stability and the reason for the continuous increase in capacity, the Mn 2p XPS spectra of Li_2MnO_3 at different cycles at 500 mA g^{-1} were compared. After the first discharge, Mn^0, Mn^{2+} and Mn^{4+} exist simultaneously (Fig. 4aIV, line A). After the first charge, however, Mn^0 disappears, corresponding to the oxidation of Mn. The amount of Mn^0 present is much less than that of Mn^{2+}, which is approximately equal to that of Mn^{4+} (Fig. 4aIV, line B). After 200 discharge/charge cycles, the XPS results show that the valency of Mn shifts toward to a higher state and the amount of Mn^0 is much less than that of Mn^{2+}, which is, in turn, less than that of Mn^{4+}, indicating that the amount of $Mn(OH)_2$ decreases and that of Li_2MnO_3 (or MnO_2) increases after long periods of cycling (Fig. 4aIV, line C). The differences in the valency of Mn during the electrochemical process can explain the increase in capacity during cycling. This is different from the MnO_2 electrode, in which the metallic Mn forms directly;[16] in the Li_2MnO_3 electrode, a mass of manganese hydroxide forms as a buffer in addition to metallic Mn. This analysis shows that the Li-enrichment can act as an electrochemical buffer on the depth of charging.

Through the crystallographic analysis, we also observed that the crystal structure changes after Li-enrichment: the volume of the cells with internal Li-enrichment (Li_2MnO_3) is 79.0% larger than that of MnO_2 with the same number of Mn atoms. These effects can alleviate the mechanical stress induced by the volume change and the aggregation of the Mn nanoparticles during cycling. It is assumed that the pre-inserted Li in the manganese oxide lattice plays a key role in the dispersion of the Mn nanoparticles embedded in the Li_2O matrix, which are expected to retain their high internal electrical contact after conversion during cycling. Thus, Li-enrichment in metal oxide anode materials can exhibit a physical buffer to volume expansion.

Conclusions

In this work, we have tried to fundamentally solve the problem of capacity fading which is observed in conversion reaction materials. This capacity fading is caused by the large amounts of Li_2O generated in the interior of the structure when the insertion of Li causes volume expansion and mechanical fracture from the inside out. We have developed a strategy to optimize the internal Li-enrichment and have successfully synthesized a novel Li_2MnO_3 nanowire anode material for LIB. Electrochemical measurements suggest that the anode material of the Li_2MnO_3 nanowires undergoing conversion reactions exhibits an excellent performance in terms of reversible specific capacity, cycling stability and rate performance. The reversible capacity can reach 1279 mA h g^{-1} at a current density of 500 mA g^{-1} after 500 cycles, much higher than those of pure MnO_2 nanowires and other commercial anode materials. Studies using XRD, modeling and photoelectron spectroscopy have shown that Li-enrichment in the metal oxide anode material plays a key role in stabilization and acts as both an electrochemical buffer during the charge–discharge cycles and as a physical buffer to volume expansion. In addition, this Li-enrichment method may remove the requirement that the cathode contains Li in its original state and opens up new avenues for pairing Li-free electrodes for the next generation of high-energy LIB. This new material and the optimization strategy will find applications in the field of energy storage.

Notes and references

1 J. M. Tarascon and M. Armand, *Nature*, 2001, **414**, 359–367.
2 B. Kang and G. Ceder, *Nature*, 2009, **458**, 190–193.
3 H. G. Jung, M. W. Jang, J. Hassoun, Y. K. Sun and B. Scrosati, *Nat. Commun.*, 2011, **2**, 516.
4 L. Ji, Z. Lin, M. Alcoutlabi and X. Zhang, *Energy Environ. Sci.*, 2011, **4**, 2682–2699.
5 L. Q. Mai, F. Yang, Y. L. Zhao, X. Xu, L. Xu, B. Hu, Y. Z. Luo and H. Y. Liu, *Mater. Today*, 2011, **14**, 346–353.
6 P. G. Bruce, B. Scrosati and J. M. Tarascon, *Angew. Chem., Int. Ed.*, 2008, **47**, 2930–2946.
7 V. Etacheri, R. Marom, R. Elazari, G. Salitra and D. Aurbach, *Energy Environ. Sci.*, 2011, **4**, 3243–3262.
8 B. Scrosati, J. Hassoun and Y. K. Sun, *Energy Environ. Sci.*, 2011, **4**, 3287–3295.
9 F. Cheng, J. Liang, Z. Tao and J. Chen, *Adv. Mater.*, 2011, **23**, 1695–1715.
10 L. Dupont, S. Laruelle, S. Grugeon, C. Dickinson, W. Zhou and J. M. Tarascon, *J. Power Sources*, 2008, **175**, 502–509.

11 M. Reddy, T. Yu, C. H. Sow, Z. X. Shen, C. T. Lim, G. Subba Rao and B. Chowdari, *Adv. Funct. Mater.*, 2007, **17**, 2792–2799.

12 K. T. Nam, D. W. Kim, P. J. Yoo, C. Y. Chiang, N. Meethong, P. T. Hammond, Y. M. Chiang and A. M. Belcher, *Science*, 2006, **312**, 885–888.

13 Y. Cui, Z. Wen and Y. Liu, *Energy Environ. Sci.*, 2011, **4**, 4727–4734.

14 F. Meng, Z. Fang, Z. Li, W. Xu, M. Wang, Y. Liu, J. Zhang, W. Wang, D. Zhao and X. Guo, *J. Mater. Chem. A*, 2013, **1**, 7235–7241.

15 Y. Yu, Y. Shi and C. H. Chen, *Nanotechnology*, 2007, **18**, 055706.

16 A. L. M. Reddy, M. M. Shaijumon, S. R. Gowda and P. M. Ajayan, *Nano Lett.*, 2009, **9**, 1002–1006.

17 F. Jiao and P. G. Bruce, *Adv. Mater.*, 2007, **19**, 657–660.

18 J. Chang, M. Jin, F. Yao, T. H. Kim, V. T. Le, H. Yue, F. Gunes, B. Li, A. Ghosh and S. Xie, *Adv. Funct. Mater.*, 2013, **23**, 5074–5083.

19 L. Peng, X. Peng, B. Liu, C. Wu, Y. Xie and G. Yu, *Nano Lett.*, 2013, **13**, 2151–2157.

20 Q. Wang, J. Xu, X. Wang, B. Liu, X. Hou, G. Yu, P. Wang, D. Chen and G. Shen, *ChemElectroChem*, 2013, **1**, 559–564.

21 L. Mai, H. Li, Y. Zhao, L. Xu, X. Xu, Y. Luo, Z. Zhang, W. Ke, C. Niu and Q. Zhang, *Sci. Rep.*, 2013, **3**, 1718–1725.

22 J. Cabana, L. Monconduit, D. Larcher and M. R. Palacín, *Adv. Mater.*, 2010, **22**, E170–E192.

23 M. Reddy, G. Subba Rao and B. Chowdari, *Chem. Rev.*, 2013, **113**, 5364–5457.

24 S. Lee, Y. Cho, H. K. Song, K. T. Lee and J. Cho, *Angew. Chem., Int. Ed.*, 2012, **51**, 8748–8752.

25 J. Guo, Q. Liu, C. Wang and M. R. Zachariah, *Adv. Funct. Mater.*, 2012, **22**, 803–811.

26 B. Sun, Z. Chen, H. S. Kim, H. Ahn and G. Wang, *J. Power Sources*, 2011, **196**, 3346–3349.

27 J. Liu and Q. Pan, *Electrochem. Solid-State Lett.*, 2010, **13**, A139–A142.

28 H. Xia, M. Lai and L. Lu, *J. Mater. Chem.*, 2010, **20**, 6896–6902.

29 Y. Shi, J. Z. Wang, S. L. Chou, D. Wexler, H. J. Li, K. Ozawa, H.-K. Liu and Y. P. Wu, *Nano Lett.*, 2013, **13**, 4715–4720.

30 F. Zou, X. Hu, L. Qie, Y. Jiang, X. Xiong, Y. Qiao and Y. Huang, *Nanoscale*, 2014, **6**, 924–930.

31 X. Gu, L. Chen, Z. Ju, H. Xu, J. Yang and Y. Qian, *Adv. Funct. Mater.*, 2013, **23**, 4049–4056.

32 Y. M. Lin, R. K. Nagarale, K. C. Klavetter, A. Heller and C. B. Mullins, *J. Mater. Chem.*, 2012, **22**, 11134–11139.

33 W. Zhou, C. Cheng, J. Liu, Y. Y. Tay, J. Jiang, X. Jia, J. Zhang, H. Gong, H. H. Hng and T. Yu, *Adv. Funct. Mater.*, 2011, **21**, 2439–2445.

34 J. Zhu, Z. Lu, M. O. Oo, H. H. Hng, J. Ma, H. Zhang and Q. Yan, *J. Mater. Chem.*, 2011, **21**, 12770–12776.

35 L. Q. Mai, F. Yang, Y. L. Zhao, X. Xu, L. Xu and Y. Z. Luo, *Nat. Commun.*, 2011, **2**, 381.

36 N. Liu, L. Hu, M. T. McDowell, A. Jackson and Y. Cui, *ACS Nano*, 2011, **5**, 6487–6493.

37 X. Xu, Y. Z. Luo, L. Q. Mai, Y. L. Zhao, Q. Y. An, L. Xu, F. Hu, L. Zhang and Q. J. Zhang, *NPG Asia Mater.*, 2012, **4**, e20.

38 M. W. Forney, M. J. Ganter, J. W. Staub, R. D. Ridgley and B. J. Landi, *Nano Lett.*, 2013, **13**, 4158–4163.

39 M. R. Lukatskaya, O. Mashtalir, C. E. Ren, Y. Dall'Agnese, P. Rozier, P. L. Taberna, M. Naguib, P. Simon, M. W. Barsoum and Y. Gogotsi, *Science*, 2013, **341**, 1502–1505.

40 R. Wang, X. He, L. He, F. Wang, R. Xiao, L. Gu, H. Li and L. Chen, *Adv. Energy Mater.*, 2013, **3**, 1358–1367.

41 X. Wang and Y. Li, *J. Am. Chem. Soc.*, 2002, **124**, 2880–2881.

42 M. Kundu, C. C. A. Ng, D. Y. Petrovykh and L. Liu, *Chem. Commun.*, 2013, **49**, 8459–8461.

43 W. M. Zhang, J. S. Hu, Y. G. Guo, S. F. Zheng, L. S. Zhong, W. G. Song and L. J. Wan, *Adv. Mater.*, 2008, **20**, 1160–1165.

44 C. Kim, N. S. Norberg, C. T. Alexander, R. Kostecki and J. Cabana, *Adv. Funct. Mater.*, 2012, **23**, 1214–1222.

45 A. R. Armstrong, C. Lyness, P. M. Panchmatia, M. S. Islam and P. G. Bruce, *Nat. Mater.*, 2011, **10**, 223–229.

46 P. Poizot, S. Laruelle, S. Grugeon, L. Dupont and J. Tarascon, *Nature*, 2000, **407**, 496–499.

47 Y. Y. Hu, Z. Liu, K. W. Nam, O. J. Borkiewicz, J. Cheng, X. Hua, M. T. Dunstan, X. Yu, K. M. Wiaderek, L. S. Du, K. W. Chapman, P. J. Chupas, X. Q. Yang and C. P. Grey, *Nat. Mater.*, 2013, **12**, 1130–1136.